Stochastic atomic acceleration during the X-ray-induced fluidization of a silica glass

Francesco Dallari[a,b,1,2], Alessandro Martinelli[b,1,2], Federico Caporaletti[c,d], Michael Sprung[a], Giacomo Baldi[e], and Giulio Monaco[b,1,2]

The X-ray-induced, nonthermal fluidization of the prototypical SiO_2 glass is investigated by X-ray photon correlation spectroscopy in the small-angle scattering range. This process is initiated by the absorption of X-rays and leads to overall atomic displacements which reach at least few nanometers at temperatures well below the glass transition. At absorbed doses of ∼5 GGy typical of many modern X-ray-based experiments, the atomic displacements display a hyperdiffusive behavior and are distributed according to a heavy-tailed, Lévy stable distribution. This is attributed to the stochastic generation of X-ray-induced point defects which give rise to a dynamically fluctuating potential landscape, thus providing a microscopic picture of the fluidization process.

XPCS | glasses | out of equilibrium systems

Recent experiments carried out using wide-angle X-ray photon correlation spectroscopy (XPCS) have revealed that X-rays in the 10-keV range induce in some oxide glasses local fluidization of the material via a nonthermal process (1–5). XPCS probes the q component of the density correlation function, $F(q,t) = \langle \rho_q^*(0)\rho_q(t) \rangle$, where q is the scattering vector and $\rho_q(t)$ is the q component of the microscopic density (6). The claim of local fluidization comes from the observation that the density correlation function at the interatomic length scale decays to zero under X-ray irradiation: This is a sign of a complete renewal of the atomic configuration typical of a liquid but not of a glass. The characteristic timescale, $\tau(q)$, of such configuration renewal turns out to be inversely proportional to the X-ray dose rate (1–5).

Atomic displacements initiated by radiation and ionizing particles in silica samples were already observed in several experiments (7–10): It is in fact well known that atomic motions can be induced via elastic and inelastic scattering (11). The possibility of measuring by XPCS the full density correlation function and thus of probing the complete fluidization process during irradiation over a range of different q values (and therefore of different length scales) can provide information useful to clarify the nature of this process. In particular, the available data show that $\tau(q)$ decreases on increasing q (1), though the limited q range investigated so far makes it unclear whether this dependence is linear (12) or rather a smoother power law (13).

Moreover, the correlation functions measured by XPCS in silica (1) display a peculiar shape tagged "compressed exponential." Compressed exponential relaxations have been reported in several systems, most notably soft materials in an arrested state, using dynamic light scattering (14–16) and small-angle XPCS (17, 18). In these studies, the occurrence of a compressed exponential shape has been recognized to be the signature of stress relaxation, where stress sources arise spontaneously in the aging material (14, 15). It is clearly tempting to describe the X-ray-induced fluidization in terms of stress relaxation, where the stress would be induced in this case by X-ray absorption; it is then crucial to investigate the q dependence of the $F(q,t)$ over a larger q range than already available and, in particular, at smaller q's in order to study how the observed local fluidization process evolves toward larger length scales. To reach this goal, we report here on an XPCS experiment that reaches the small angle, low-q range of a glass of silica. This range is notoriously difficult to investigate for atomic glasses due to the low scattering rate. The present data cover almost two decades in q from the small-angle X-ray scattering (SAXS) to the wide-angle X-ray scattering (WAXS) range. They clarify that, for absorbed doses of ∼5 GGy typical of many modern X-ray-based experiments, the atomic displacements that follow X-ray irradiation are distributed according to a Lévy stable law and result from stochastic acceleration, revealing important aspects of the X-ray-induced fluidization process.

The XPCS measurements were carried out using two acquisition schemes corresponding to two different average dose rates: 2 s (1.5 s) of exposure per frame

Significance

Upon X-ray irradiation, a number of glasses undergo a fluidization process: The atoms move from their original positions while keeping a similar distribution of interatomic distances, as for two snapshots of a liquid. This process has been studied looking at the atomic displacements over interatomic distances. We here extend these investigations to much longer length scales in the few nanometer range. For silica irradiated at doses of ∼5 GGy, our experiments clarify that this process is not characterized by the common atomic diffusion typical of liquids: It is rather the outcome of an atomic acceleration due to X-ray-induced local stresses random in both time and space, as in the famous example of stochastic acceleration of charged particles by interstellar fields.

[1]F.D., A.M., and G.M. contributed equally to this work.

[2]To whom correspondence may be addressed. Email: francesco.dallari@unipd.it, alessandro.martinelli@unipd.it, or giulio.monaco@unipd.it.

with no (3 s) waiting time between frames. They will be referred to in the following as high dose rate (HDR) and low dose rate (LDR), respectively. The corresponding average dose rate values, calculated assuming an elliptical cross-section for the beam with major and minor semiaxes equal, along the horizontal and vertical directions, to the corresponding FWHM/$\sqrt{2\ln(2)}$ values, are 7.8 (2.6) MGy/s for the HDR (LDR) runs. In the case of SiO_2, the scattered intensity in the small-angle range is more than one order of magnitude smaller than at the maximum of the scattered intensity. The combination of low count rates and long relaxation times required acquisition times of ∼40 min (2 h) for the HDR (LDR) measurements.

For each measurement scheme, the detector images were divided into regions of interest (ROI) defined by the q intervals selected for the analysis. The scattered intensity, $I(q)$, was obtained from individual images, while a two-times correlation matrix was calculated as follows:

$$C_q(t_1, t_2) = \frac{\langle (I_p(t_1) - \langle I_p(t_1) \rangle)(I_p(t_2) - \langle I_p(t_2) \rangle) \rangle}{\langle I_p(t_1) \rangle \langle I_p(t_2) \rangle}, \quad [1]$$

where $I_p(t)$ is the intensity collected by pixel p at time t in the q-ROI, and $\langle \ldots \rangle$ indicates average over the pixels belonging to that ROI. Eq. 1 can be alternatively expressed as function of the waiting time $t_w = t_1$ and lag-time $t = t_2 - t_1$. Then, averaging $C_q(t_w, t_w + t)$ over an appropriate range of t_w, the normalized intensity correlation function $g_2(q, t) = 1 + C|F(q, t)|^2$ can be computed, *SI Appendix* for more details. Here, C is an instrumental constant known as contrast (6). The obtained $g_2(q, t)$ was then described using for $|F(q, t)|^2$ the expression (14):

$$|F(q, t)|^2 = \exp[-2(t/\tau(q))^{\beta(q)}], \quad [2]$$

where $\beta(q)$ is the shape parameter.

In Fig. 1*A*, the scattered intensity is reported as a function of q. It is possible to identify two regimes: the first, at lower q's, where the intensity drops very rapidly, and the second, at larger q's, where the intensity is almost q independent; *SI Appendix* for more details. The low-q regime originates from the roughness of the surfaces (19).

This roughness scattering follows a power law behavior described by $I_s^0 q^{-\delta}$, where I_s^0 is a constant. The second regime corresponds to the intensity scattered from the bulk in the $q \to 0$ limit (20). In this regime, the scattered intensity depends weakly on q and can be treated as a constant, I_b^0. The measured $I(q)$ can then be described as follows:

$$I(q) = I_s^0 q^{-\delta} + I_b^0. \quad [3]$$

This expression indeed accurately fits the experimental data, as shown in Fig. 1*A*. Noticeably, according to the model of Eq. 3, for $q > 0.34$ nm^{-1}, bulk scattering dominates the scattered intensity; see *Inset* of Fig. 1*A*. Clearly, there is no sharp transition between the surface- and the bulk-dominated scattering range, and the quoted q value marks simply a point where the two contributions are roughly comparable.

In Fig. 1*B*, the normalized $g_2(q, t) - 1$ data corresponding to the LDR run are reported for selected q's. Lower q's correspond to longer relaxation times; correlation functions corresponding to $q \leq 0.2$ nm^{-1} do not show a complete decorrelation in the probed time window and are not plotted. For $q < 0.34$ nm^{-1}, $\tau(q)$ essentially corresponds to the time required for a complete renewal of the surface roughness. This shows that X-ray irradiation induces not only local fluidization of the bulk but of the surface as well.

The q dependence of the intensity correlation function can be captured looking at the relevant parameters obtained by fitting Eq. 2 to the experimental data. One key point, however, is that the data discussed here show a complex dose and dose rate dependence that has to be disentangled. The dose rate dependence has been discussed in previous studies, where it was shown that the decay time of the intensity correlation functions
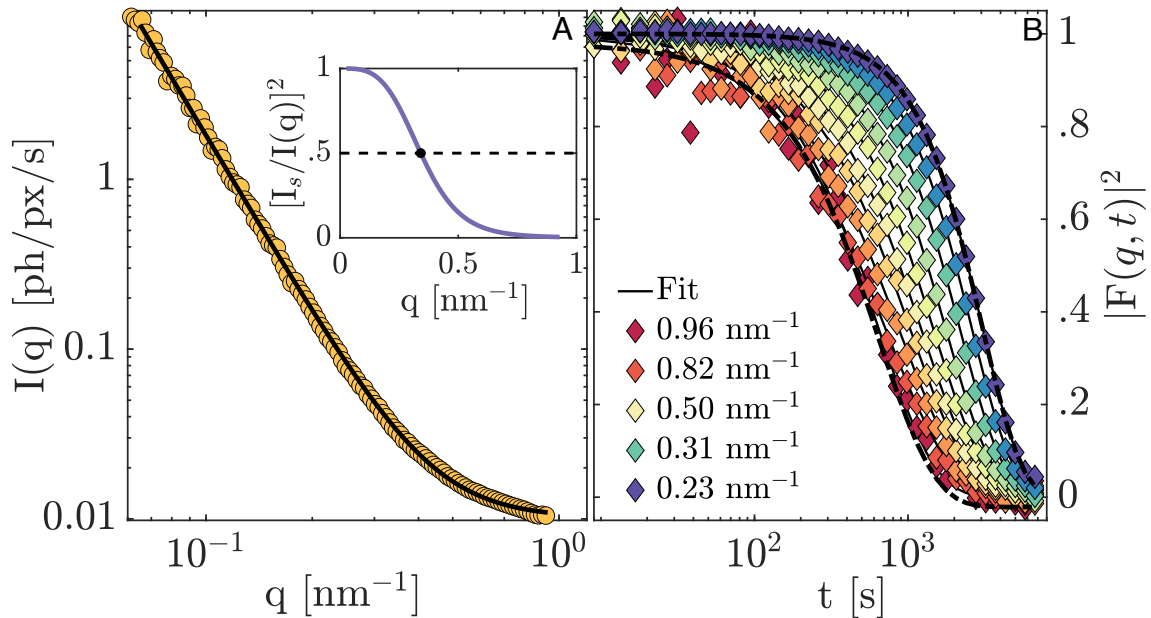
Fig. 1. (*A*) Scattered intensity collected in the LDR run (symbols) together with the best-fitting curve of Eq. 3 (line); the fit parameters are $I_s^0 = (8.6 \pm 0.1) \cdot 10^{-4}$ ph/s/nm$^\delta$, $\delta = 3.5 \pm 0.1$ and $I_b^0 = (15.20 \pm 0.01) \cdot 10^{-3}$ ph/s. *Inset*, Ratio of the square of the surface-scattered intensity to the total one. The horizontal line shows that for $q > 0.34$ nm^{-1}, scattering from the bulk dominates. (*B*) Normalized intensity correlation functions for the LDR series at various q's from 0.23 to 0.96 nm^{-1} (blue to red) together with two examples of the best-fitting functions of Eq. 2 (lines). In all panels, the data are averaged over all collected images.

scales with the inverse of the dose rate (1–5). For what concerns the dose dependence, in the *Inset* of Fig. 2A a $C_q(t_1, t_2)$ matrix is reported for the HDR series and for $q = 0.64$ nm^{-1}. It is possible to see there a small increase in the relaxation time with dose (age), as typically observed in aging materials; see e.g., refs. 21 and 22.

In Fig. 2A, the relaxation time, $\tau(q)$, extracted from the HDR series at two representative waiting times is reported as a function of q. In both cases, $\tau(q)$ decreases on increasing q, but at lower q's, the dynamics slows down fast with sample age. At higher q's, the two datasets are instead closer.

The corresponding shape parameters, $\beta(q)$, are reported in Fig. 2B. At short waiting time, the data are constant and compatible with the values observed in wide-angle scattering measurements, where it was found that $\beta = 1.40 \pm 0.12$ (1) (gray stripe). These wide-angle scattering data correspond close to the peak of the scattered intensity, to a dose of ~5 GGy. The q independence of $\beta(q)$ over more than a decade in q shown in Fig. 2B is remarkable and recalls similar results obtained in light-scattering studies of stress relaxation (14–16); moreover, the values of β obtained in those experiments are also very close to the ones found here. In the data at longer waiting time, instead, the shape parameter decreases at high q's. This might be related to the structural changes that appear in the glass at the corresponding doses (1).

To compare the present results with those in the literature (1), it is then necessary to evaluate the data at the same dose, D, and then scale them to the same dose rate, d_r (2, 5). In particular, the computation of correlation functions intrinsically relies on

information at different ages (and thus doses). However, starting from a $C_q(t_w, t_w + t)$ matrix, only patterns up to $\sim t_w + \tau$ give a relevant contribution to the correlation function for a given t_w. The dose–t_w relation can then be taken as $D = d_r \cdot (\tau + t_w)$. It is then possible, selecting the appropriate waiting times t_w, to interpolate the values of the relaxation times for the HDR and LDR series at a dose of 5 GGy, thus obtaining the data $\tau_5(q)$ reported in Fig. 3A. In Fig. 3B, the ratio between the $\tau_5(q)$ data derived from the HDR and LDR series is reported. This is one of the hallmarks of the induced dynamics: This ratio matches the inverse ratio of the corresponding dose rates, confirming previous observations (1, 2).

Given the proportionality of the relaxation time to the inverse dose rate for a total dose of 5 GGy, it is now possible to compute a relaxation time, $\tau_5^R(q)$, scaled to the dose rate used in the HDR series and in the dose limit of 5 GGy from the measurements carried out in both LDR and HDR conditions. In Fig. 4, these data are reported together with additional wide-angle scattering control measurements at the same dose and scaled to the same dose rate and described in more detail in *SI Appendix*. The results from the present experiment can be described as $\tau_5^R(q) = 1/(bq^\alpha)$ (dashed line in Fig. 4), with $\alpha = 0.56 \pm 0.04$ and $b = (299 \pm 9) \cdot 10^{-5}$ nm$^\alpha$s^{-1}. Remarkably, the same power law is also well in line with the literature data from wide-angle experiments (1) scaled to the same dose rate, though an additional multiplication factor of 1.1 was applied here. Such a small correction factor is likely a residual systematic error in the comparison of absolute intensities at different beamlines (P10 at
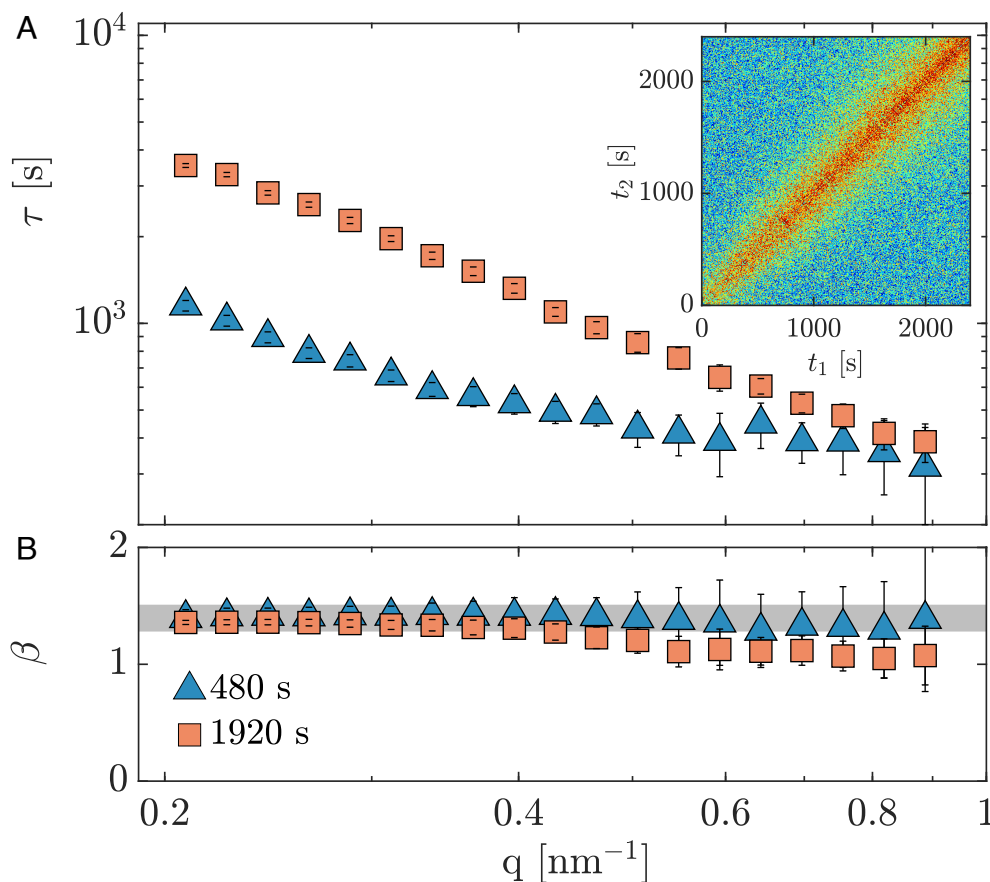
Fig. 2. (A) q dependence of the relaxation time, $\tau(q)$, for the HDR series and at the waiting times indicated in the legend. *Inset*: Two-times correlation matrix corresponding to the HDR series and $q = 0.64$ nm^{-1}. (B) q dependence of the shape parameter, β, for the same data as in (A). The range of values observed in wide-angle scattering measurements (1) is also reported (gray stripe).

3 of 7
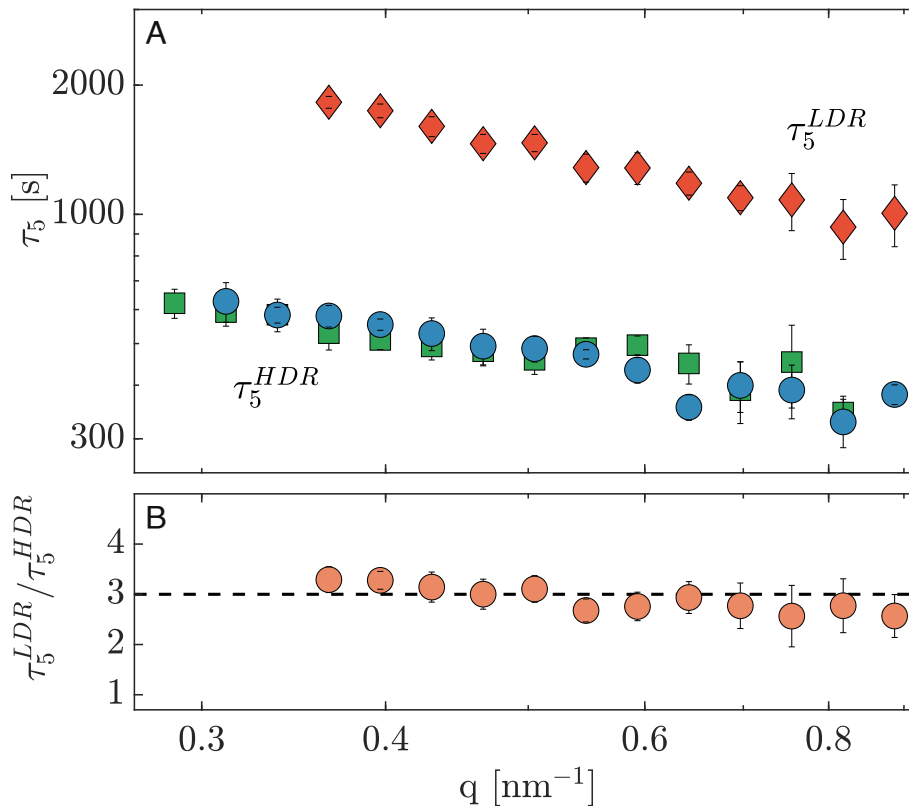
Fig. 3. (*A*) The relaxation times interpolated at a dose of 5 GGy are reported for the LDR (diamonds) and two HDR runs (circles and squares). (*B*) *q* dependence of the ratio of the LDR and HDR relaxation times reported in (*A*). This ratio matches the inverse ratio of the corresponding dose rates (dashed line).

Petra for the present measurements and ID10 at the ESRF for those from ref. 1).

It is interesting to observe that, while the *q* dependence of the $I(q)$ data reported in Fig. 1 clearly suggests the presence of two different scattering contributions, from the surface roughness and from the bulk, the $\tau_5^R(q)$ data reported in Fig. 4 rather suggest a single mechanism active in the whole *q* range. In other terms, Fig. 4 suggests that the same microscopic mechanism following
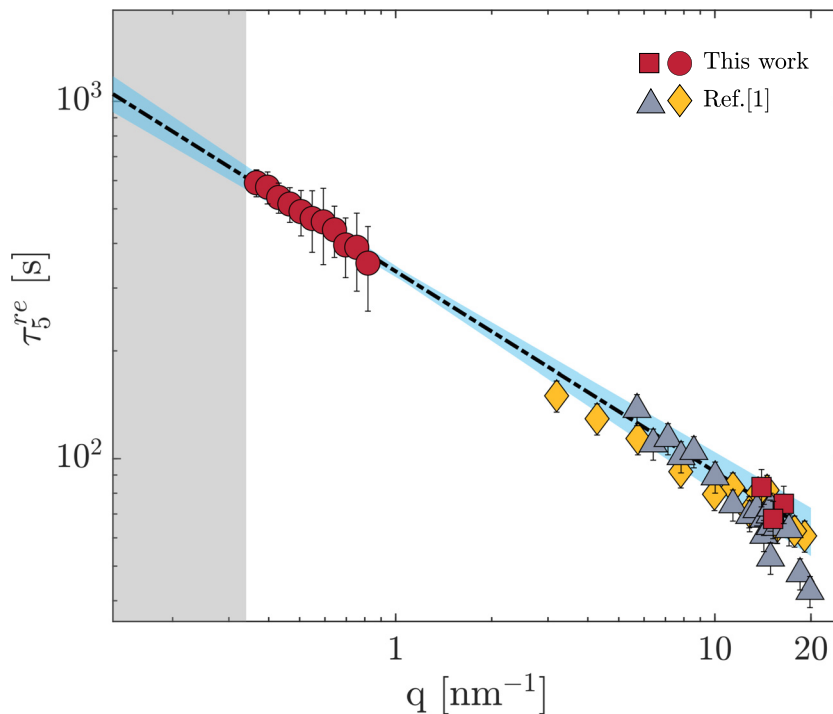
Fig. 4. Relaxation times as a function of *q* rescaled to a dose rate of 7.8 MGy/s for the small-angle scattering data (circles) together with three control measurements at high *q* (squares) and the data from ref. 1 (diamonds and triangles). The data from ref. 1 have been additionally multiplied by a factor 1.1. All data correspond to a dose of 5 GGy. The dashed line is the best-fitting function $\tau_5^R(q) = 1/(bq^\alpha)$.

X-ray absorption acts to change the atomic configuration in the bulk of the glass as well as at its surface.

The results reported in Figs. 2B and 4 are striking at the first sight. They can be summarized as follows:

$$F(q,t) = e^{-(b^\gamma t^\gamma q)^p}, \qquad [4]$$

where $\gamma = 1/\alpha = 1.79 \pm 0.13$ and $p = \alpha \cdot \beta(q) = 0.78 \pm 0.09$ turns out to be q independent. This is very different from a standard diffusion process where $F(q,t) = e^{-D_0 q^2 t}$, with D_0 the diffusion coefficient (23).

Eq. 4 can actually be used to infer the X-ray-induced distribution of the atomic displacements, $\Delta R(t)$, at time t. Approximating $F(q,t)$ with its self-component (23), in fact, it is possible to write

$$F(q,t) = \langle e^{i\mathbf{q}\cdot\Delta\mathbf{R}(t)} \rangle = \int g(\Delta\mathbf{R}(t))e^{i\mathbf{q}\cdot\Delta\mathbf{R}(t)} \, d(\Delta\mathbf{R}), \quad [5]$$

where $g(\Delta\mathbf{R}(t))$ is the distribution function of $\Delta\mathbf{R}(t)$ at time t. Using Eq. 4 and following ref. 15, it is then possible to invert Eq. 5 to extract $g(\Delta\mathbf{R}(t))$ or, rather, the function $w(\Delta\mathbf{R}(t)) = 4\pi^2(\Delta R(t))^2 g(\Delta\mathbf{R}(t))$, which represents the distribution function of the modulus of $\Delta\mathbf{R}(t)$. The result is

$$w(\Delta R(t)) = -\frac{2\Delta R(t)}{(bt)^\gamma}\frac{d}{d(\Delta R)}L_{p,0}(\Delta R/(bt)^\gamma), \qquad [6]$$

where $L_{p,0}$ is the Lévy stable law, characterized by an asymptotic power law decay: $L_{p,0} \sim (\Delta R)^{-(p+1)}$ (15, 23).

Eq. 6 allows evaluating $w(\Delta R(t))$ at different times. It only depends on the parameter b, which, as remarked earlier, is proportional to the dose rate. In Fig. 5, we report $w(\Delta R(t))$ at times $t = \tau(q = 15.2 \text{ nm}^{-1}) = 67$ s and $t = \tau(q = 0.37 \text{ nm}^{-1}) = 590$ s, i.e., at times corresponding to the decay time of the intensity correlation function at the maximum and minimum q values reached in the present experiment (shortest and longest decay times, respectively). We underline here that both curves correspond to the same dose of 5 GGy and to the HDR case. The gray area in Fig. 5 corresponds to the q range directly explored by us: Smaller and larger displacements can be estimated only by extrapolation.

The Lévy distribution features an infinite variance; when used to describe experimental data, this is often dealt with truncating it at some cutoff value (24–27). In these cases, the variance of the distribution remains finite and scales as $\langle(\Delta\mathbf{R})^2\rangle \sim t^{2\gamma}$ (24–26). However, it is still possible to evaluate the most probable displacement, ΔR^*, identified by the maximum of $w(\Delta R(t))$ (the mode of the distribution). The most probable displacements for the distributions reported in Fig. 5 are 0.037 and 1.75 nm, respectively, and are close to $\sim 1/q$ in both cases. The values of ΔR^*, evaluated at times corresponding to the relaxation times probed in the present experiment, are reported in the *Inset* of Fig. 5, where it is also shown that $\Delta R^* \propto t^\gamma$. In other terms, the mode of the distribution function scales as the root mean square displacement calculated with some reasonable cutoff.

At this point, it is interesting to compare the distribution functions $w(\Delta R)$ that we observe for the present case of irradiation-induced dynamics with that corresponding to a simple diffusive dynamics to better grasp the consequences of the process at play here. Simple diffusion can be described by Eq. 4 with parameters $p = 2$ and $\gamma = 0.5$. The corresponding distribution $w(\Delta R)$ can be readily calculated using again Eq. 6.
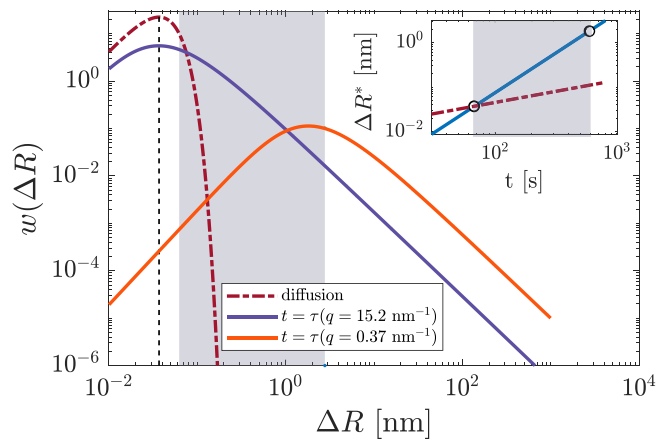
Fig. 5. Main panel: Distribution functions of atomic displacements, $w(\Delta R)$, for a SiO_2 glass irradiated with a dose rate of 7.8 MGy/s (HDR) and for a total dose of 5 GGy calculated at times corresponding to the relaxation times, $\tau(q)$, at the highest (blue line) and shortest (orange line) q values probed in the present XPCS experiment. The gray-shaded area highlights the reciprocal of the range, where, in q space, our experiment has been carried out. The black dashed vertical line indicates the position of the most probable displacement (the mode of the distribution) for the large-q case. The brown dot-dashed line is the distribution $w(\Delta R)$ calculated for a diffusive dynamics, and the value of the diffusion coefficient, D_0, is chosen to match the mode of the distribution to that of the distribution for the induced dynamics for the largest probed q. Inset, Time dependence of the mode, ΔR^*, of the distribution of atomic displacements probed under irradiation at times corresponding to the measured $\tau(q)$ (circles). This time dependence is well described by a power law $\Delta R^* \propto t^\gamma$ with $\gamma = 1.79$ (blue line). Very different is the case of the simple diffusion process (red dot-dashed line), where $\Delta R^* \propto t^{0.5}$.

It can be compared to the one characteristic of the irradiation process at a given time by matching the mode of the two distributions by an appropriate choice of the diffusion coefficient, as shown in Fig. 5 for a time of 67 s. The distribution function for the simple diffusion case (red dash-dotted line) shows the well-known exponential decay, signifying that long displacements are exponentially less likely. This is clearly different from the situation which is reached upon irradiation, where the heavy tail of the distribution of atomic displacements indicates a high probability for large displacements. As shown in the *Inset* of Fig. 5, in addition to this heavy tail, the mode of the distribution for the irradiation-induced displacements increases with time much faster than that for simple diffusion, where $\Delta R^* \propto t^{0.5}$.

We note on passing that the diffusion coefficient used in Fig. 5 to match the two distributions to the same mode is $D_0 = 5 \cdot 10^{-22}$ cm^2/s, which is a very small value. This is the diffusion coefficient known for SiO_2 at temperatures around the glass transition (28). This is consistent with the fact that a relaxation time of 67 s is indeed typical of a glass close to the glass transition temperature. In other terms, the most probable atomic displacement induced by an X-ray beam with a dose rate of 7.8 MGy/s and at a dose of 5 GGy is close to that of SiO_2 at the glass transition temperature.

The comparison between the distribution function of the atomic displacements for simple diffusion and for the irradiation-induced dynamics suggests a natural way to identify the anomalously long displacements which appear under irradiation. We can call in fact "long displacements" those that are not likely to be reached in a simple diffusion process. They can be evaluated computing the cumulative distribution functions (cdf) for the two distributions. We can call "long displacements" those larger than the displacement at which the cdf for the mode-matching distribution for simple diffusion is 0.99. For

that value of displacement, the cdf for the irradiation-induced dynamics is 0.36, meaning that, for the Lévy stable distribution that we probe under irradiation, 64% of the displacements can be considered long or that for each "short" displacement, there are approximately 2 "long" ones. These numbers are useful to provide a qualitative picture of the dynamics induced by irradiation though they are clearly arbitrary as they depend on the threshold used to define an unlikely event for the simple diffusion case. This however does not change the qualitative conclusion that during the irradiation-induced dynamics studied here, a relevant fraction of the atomic displacements are out of reach for a simple diffusion process.

In order to rationalize our findings, it is useful to discuss the microscopic origin of the fluidization process taking place under X-ray irradiation. In SiO_2, the most likely event following the absorption of a hard X-ray photon is the generation of a photoelectron from the Si K-shell and then of a cascade of secondary electrons. A fraction of these electrons will give rise to self-trapped excitons which, in wide band gap materials, couple efficiently to the atomic positions. The final result of the self-trapped excitons generation and decay is the build-up of a population of point defects, e.g., associated with broken Si-O bonds (29). These defects act as local stress sources in the glass and more specifically provide dipolar sources of stress (30). We are then in the presence of a random distribution of local stress sources that fluctuate both in space and in time.

The problem of particle displacements in an evolving random potential has been studied theoretically in some detail as it can increase the transport rate beyond diffusion, where, as we have just seen, $\langle (\Delta \mathbf{R})^2 \rangle \propto t$, and even beyond ballistic transport, where $\langle (\Delta \mathbf{R})^2 \rangle \propto t^2$ (31–33). In particular, hypertransport is observed on a timescale longer than that characteristic of the evolving random potential but slower than that associated with friction. In the present case, the former scale is fixed by the inverse of the X-ray absorption rate while the latter one must be very long as we are dealing with a glass in the elastic limit, where friction is negligible. There is then plenty of scope here for realizing conditions for hyperdiffusion. A good explanation of our data is then provided by an extreme case of hypertransport, where particles are stochastically accelerated with the prediction that $\langle (\Delta \mathbf{R})^2 \rangle \propto t^3$ (31–33). Our result for $2\gamma = 3.6 \pm 0.3$ is compatible with such a prediction within two standard deviations. This regime is well known in other contexts as for the case of acceleration of charged particles by interstellar fields (34) and for light propagating through a photonic medium containing spatial disorder fluctuating in time (35). The present results provide an example of stochastic acceleration of atoms by fluctuating stress fields.

A random distribution of stress sources is however expected to give rise to a distribution $w(\Delta R) \sim (\Delta R)^{-5/2}$ (15, 36). This is sensibly different from what we observe here, where $w(\Delta R) \sim (\Delta R)^{-1.78}$: in SiO_2 irradiated at 5 GGy, $w(\Delta R)$ shows a heavier tail than expected, implying a larger probability for atomic displacements at larger distances. This might be interpreted as a sign that, at the considered dose, the population of point defects generated in the glass is dense enough to modify the displacement field expected for a random distribution of elastic dipoles in the far field limit.

While more experiments will have to be carried out to better clarify this discrepancy, it is interesting to reflect on possible reasons for that. We could for instance imagine a "facilitation" scenario, a concept of relevance in the physics of glasses and undercooled liquids (37, 38), where the proximity of fluidized regions might facilitate larger displacements. Given the figures reported in *Materials and Methods* for the beam intensity, its spot size and energy, and the sample thickness, we can estimate that $\simeq 20$ photons/($\mu m^3 \mu s$) are absorbed in our SiO_2 sample. In order for a facilitation mechanism to be effective, the atomic rearrangements triggered by one photon should last order of a microsecond over volumes of the order of a cubic micrometer to affect the rearrangements induced by a second photon absorbed in the vicinity. This seems unlikely. For example, if the generation of a self-trapped exciton is the main microscopic mechanism at the basis of the observed effect, the timescale of the process is indeed of the order of a microsecond (at room temperature) (39), but atomic relaxation takes place at the interatomic scale (29), maybe affecting a volume of up to a nanometer in size. There might be however a second mechanism where facilitation could intervene. The self-trapped excitons, on decaying, will normally leave a local defect in the glass matrix and thus a source of local stress. The population of defects will increase upon irradiation until, at a certain point, for a newly generated photoelectron, it will be likely to encounter an already stressed network spot. The time required for this to happen, at the dose rates explored here, might be of order 100 s if we assume that a self-trapped exciton stresses order 1 nm^3 of glass structure and that every absorbed photon generates a self-trapped exciton. The dynamics induced at this spot might then be characterized by much larger displacements and result in the observed hypertransport. At this stage, this picture remains however hypothetical and based on bold figures, and more studies are required to understand whether it can really stand scrutiny.

In conclusion, the observation of a Lévy distributed atomic displacement field provides information on the fluidization of SiO_2 under an X-ray beam. Clearly, the mechanism, based on stochastic acceleration, is completely different from that of thermal melting. XPCS shows then a clear sensitivity not only to the generation of point defects in the glass matrix but also to the response of the elastic medium, and the full development of this capability might shed light on the effects of radiation on glasses.

Materials and Methods

Experimental Set-Up. The main experiment was performed at beamline P10 of the PETRA III storage ring in Hamburg (D) in small-angle scattering configuration (40). The 8-keV X-ray beam was monochromatized using a Si(111) channel-cut crystal, and its spatially coherent part was focused onto a 3×2-μm^2 spot (FWHM) at the sample position, with an incident flux of $F_0 \simeq 4 \cdot 10^{10}$ photons/s. The SiO_2 sample, a disk of fused silica (Suprasil) 150-μm thick, was mounted in transmission geometry and held in vacuum at ambient temperature. The detector was an EIGER 4M (2,070 × 2,167 pixels, 75-μm pixel size) placed in the forward direction at 5.05 m downstream of the sample.

Sample Preparation. Disks of pure anhydrous silica (suprasil) were obtained from a larger block of silica (suprasil). The disks were ground with sandpaper down to a thickness corresponding to one absorption length for an 8-keV X-ray beam. The sample's surfaces were then polished with finer sandpaper of grit P1200 (average grain size of about 15 μm). The sample thickness was determined by X-ray transmission using a photodiode.

The final polishing of the sample's surfaces does not prevent the presence of some sharp scratches (visible also with an optical microscope). The presence of such scratches produces strong streaks of X-rays on the detector which complicate the intensity correlation analysis. To mitigate this problem, we carefully chose a

spot on the sample where the surface was as flat as possible and then masked the remaining streaks on the detector during the data analysis phase.

Author affiliations: [a]Deutsches Elektronen-Synchrotron DESY, 22607 Hamburg, Germany; [b]Dipartimento di Fisica e Astronomia "Galileo Galilei", Università degli Studi di Padova, 35131 Padova, Italy; [c]Van der Waals-Zeeman Institute, Institute of Physics, University of Amsterdam, 1098XH Amsterdam, the Netherlands; [d]Van't Hoff Institute for Molecular Sciences, University of Amsterdam, Science Park 904, 1098XH Amsterdam, the Netherlands; and [e]Department of Physics, University of Trento, 38123 Povo, Italy

1. B. Ruta *et al.*, Hard x-rays as pump and probe of atomic motion in oxide glasses. *Sci. Rep.* **7**, 396 (2017).
2. G. Pintori, G. Baldi, B. Ruta, G. Monaco, Relaxation dynamics induced in glasses by absorption of hard X-ray photons. *Phys. Rev. B* **99**, 224206 (2019).
3. K. Holzweber, C. Tietz, T. Michael Fritz, M. Sepiol, B. Leitner, Beam-induced atomic motion in alkali borate glasses. *Phys. Rev. B* **100**, 214305 (2019).
4. A. Martinelli *et al.*, Probing the dynamics of B2O3 across the glass transition: An X-ray photon correlation spectroscopy study. *Philos. Mag.* **100**, 2636–2645 (2020).
5. G. Pintori *et al.*, X-ray induced dynamics in borate glasses with different network connectivity. *Phys. Rev. B* **105**, 104207 (2022).
6. F. Lehmkuhler, W. Roseker, G. Grubel, From femtoseconds to hours–measuring dynamics over 18 orders of magnitude with coherent X-rays. *Appl. Sci.* **11**, 6179 (2021).
7. P. M. Ajayan, S. Iijima, Electron-beam-enhanced flow and instability in amorphous silica fibres and tips. *Philos. Mag. Lett.* **65**, 43–48 (1992).
8. S. G. Mayr, Y. Ashkenazy, K. Albe, R. S. Averback, Mechanisms of radiation-induced viscous flow: Role of point defects. *Phys. Rev. Lett.* **90**, 55505 (2003).
9. K. Zheng *et al.*, Electron-beam-assisted superplastic shaping of nanoscale amorphous silica. *Nat. Comm.* **1**, 24 (2010).
10. P. Y. Huang *et al.*, Imaging atomic rearrangements in two-dimensional silica glass: Watching silica's dance. *Science* **342**, 224–227 (2013).
11. D. L. Griscom, Self-trapped holes in pure-silica glass: A history of their discovery and characterization and an example of their critical significance to industry. *J. Non-Cryst. Solids* **352**, 2601–2617 (2006).
12. Y. Chushkin, Deciphering the intrinsic dynamics from the beam-induced atomic motions in oxide glasses. *J. Synchrotron Rad.* **27**, 1247–1252 (2020).
13. F. Dallari, G. Pintori, G. Baldi, A. Martinelli, B. Ruta, M. Sprung, G. Monaco. X-rays induced atomic dynamics in a lithium-borate glass. *Condens. Matter Phys.* **22**, 43606 (2019).
14. L. Cipelletti, S. Manley, R. C. Ball, D. A. Weitz, Universal aging features in the restructuring of fractal colloidal gels. *Phys. Rev. Lett.* **84**, 2275–2278 (2000).
15. L. Cipelletti *et al.*, Universal non-diffusive slow dynamics in aging soft matter. *Faraday Discuss* **123**, 237–251 (2003).
16. A. Duri, L. Cipelletti, Length scale dependence of dynamical heterogeneity in a colloidal fractal gel. *Europhys. Lett.* **76**, 972–978 (2006).
17. H. Guo *et al.*, Nanoparticle motion within glassy polymer melts. *Phys. Rev. Lett.* **102**, 075702 (2009).
18. F. Dallari *et al.*, Microscopic pathways for stress relaxation in repulsive colloidal glasses. *Sci. Adv.* **6**, eaaz2982 (2020).
19. J. A. Williams, G. E. Rindone, H. A. McKinstry, Small-angle X-ray scattering analysis of nucleation in glass: I, matrix scattering and sample surface effects. *J. Am. Ceramic Soc.* **64**, 697–702 (1981).
20. C. Levelut *et al.*, In situ measurements of density fluctuations and compressibility in silica glasses as a function of temperature and thermal history. *Phys. Rev. B* **72**, 224201 (2005).
21. B. Ruta *et al.*, Atomic-scale relaxation dynamics and aging in a metallic glass probed by X-ray photon correlation spectroscopy. *Phys. Rev. Lett.* **109**, 165701 (2012).
22. A. Jain *et al.*, Anisotropic and heterogeneous dynamics in an aging colloidal gel. *Soft Matter* **16**, 2864–2872 (2020).
23. B. J. Berne, R. Pecora, *Dynamic Light Scattering with Applications to Chemistry Biology and Physics* (Dover, New York, 2000).
24. R. N. Mantegna, H. Eugene Stanley, Stochastic process with ultraslow convergence to a Gaussian: The truncated lévy flight. *Phys. Rev. Lett.* **73**, 2946–2949 (1994).
25. I. Koponen, Analytic approach to the problem of convergence of truncated lévy flights towards the Gaussian stochastic process. *Phys. Rev. E* **52**, 1197–1199 (1995).
26. R. Matsushita, P. Rathie, S. Da Silva, Exponentially damped lévy flights. *Phys. A: Stat. Mech. Appl.* **326**, 544–555 (2003).
27. V. Zaburdaev, S. Denisov, J. Klafter, Lévy walks. *Rev. Mod. Phys.* **87**, 483–530 (2015).
28. M. Nascimento, E. Zanotto, Diffusion processes in vitreous silica revisited. *Phys. Chem. Glasses - Eur. J. Glass Sci. Technol. Part B* **48**, 08 (2007).
29. S. Ismail-Beigi, S. G. Louie, Self-trapped excitons in silicon dioxide: Mechanism and properties. *Phys. Rev. Lett.* **95**, 156401 (2005).
30. S. Bonfanti, R. Guerra, C. Mondal, I. Procaccia, S. Zapperi, Elementary plastic events in amorphous silica. *Phys. Rev. E* **100**, 60602 (2019).
31. L. Golubović, S. Feng, F.-A. Zeng, Classical and quantum superdiffusion in a time-dependent random potential. *Phys. Rev. Lett.* **67**, 2115–2118 (1991).
32. M. N. Rosenbluth, Comment on "classical and quantum superdiffusion in a time-dependent random potential". *Phys. Rev. Lett.* **69**, 1831 (1992).
33. E. Arvedson, M. Wilkinson, B. Mehlig, K. Nakamura, Staggered ladder spectra. *Phys. Rev. Lett.* **96**, 030601 (2006).
34. E. Fermi, On the origin of the cosmic radiation. *Phys. Rev.* **75**, 1169–1174 (1949).
35. L. Levi, Y. Krivolapov, S. Fishman, M. Segev, Hyper-transport of light and stochastic acceleration by evolving disorder. *Nat. Phys.* **8**, 912–917 (2012).
36. S. Chandrasekhar, Stochastic problems in physics and astronomy. *Rev. Mod. Phys.* **15**, 1–89 (1943).
37. L. O. Hedges, R. L. Jack, J. P. Garrahan, D. Chandler, Dynamic order-disorder in atomistic models of structural glass formers. *Science* **323**, 1309–1313 (2009).
38. D. Chandler, J. P. Garrahan, Dynamics on the way to forming glass: Bubbles in space-time. *Ann. Rev. Phys. Chem.* **61**, 191–217, PMID: 20055676 (2010).
39. K. Tanimura, T. Tanaka, N. Itoh, Creation of quasistable lattice defects by electronic excitation in sio_2. *Phys. Rev. Lett.* **51**, 423–426 (1983).
40. P10 coherence applications beamline (2022). http://photon-science.desy.de/facilities/petra_iii/beamlines/p10_coherence_applications. Accessed 16 December 2022.
41. F. Dallari, A. Martinelli, F. Caporaletti, M. Sprung, G. Baldi, G. Monaco, data for "Stochastic atomic acceleration during the X-ray-induced fluidization of a silica glass." Research Data UNIPD. https://researchdata.cab.unipd.it/798/. Deposited 21 December 2022.